Chapter 9

Fracture Mechanics Analysis of Face/Core Debonds

The superior performance of light-weight sandwich structures requires that the face sheets be successfully bonded to the core. Lack of bonding, or inadequate bonding, will compromise the transfer of shear stress between the face and core, and if debonding occurs over a large area, the debond is likely to grow further. It is also obvious that the face/core adhesion may vary in a large panel with composite face sheets due to inadequate wet-out of the face fabrics resulting in "islands" of poor face/core bonding. Service loads are also known to be a potential source for face/core debonding, in particular wave-slamming loads on the bottom of a ship hull or hard object impact loads transverse to the surface of a sandwich structure.

The face/core interface in a sandwich panel may be toughened by the addition of a thin low fiber content fabric layer such as a continuous fiber mat (CFM) or a chopped strand mat (CSM). Such a mat will provide a transition zone between the high modulus face sheets and the low modulus core and may improve the face/core adhesion. The preparation of the core bonding surfaces is also very important, as discussed by Pfund (2005). Ideally, the critical link for the separation of the face and core should not be the actual interface between face and core. If the adhesive layer is strong and tough, debonding tends to occur in the face sheet in the form of delamination or inside the core, see the scheme in Figure 9.1.

The morphology of the face/core interface is thus an important factor. The actual morphology depends of the core material and the manner in which the face sheets are attached to the core. For example, if fiber composite faces are used, fabric preforms may be injected with resin, forming the face sheets and the face/core bond simultaneously creating an integral, co-cured sandwich structure (Advani and Sozer, 2002). Alternatively, preformed composite or metal faces may be attached to the core using adhesive bonding procedures.

L.A. Carlsson and G.A. Kardomateas, *Structural and Failure Mechanics of Sandwich Composites*, Solid Mechanics and its Applications 121, DOI 10.1007/978-1-4020-3225-7_9,

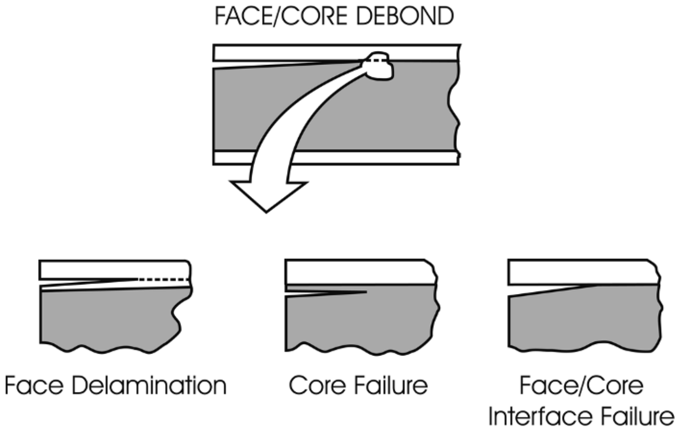

Figure 9.1 Crack growth scenarios in foam core sandwich.

The face/core debond is commonly represented as a sharp discontinuity, i.e. a crack, and the condition when this crack will propagate are analyzed using fracture mechanics principles. This chapter aims to review the fracture mechanics of face/core interface cracks and analysis of the crack path in sandwich-test specimens. For sandwich specimens that fail after developing large fiber bridging zones behind the crack tip, linear elastic fracture mechanics becomes inadequate and cohesive zone models may better represent the fracture process.

9.1 Linear Elastic Fracture Mechanics Concepts

Fracture mechanics is a science developed to analyze the tendency for a pre-existing crack in a structure to grow as a result of applied external loads. The presence of a crack reduces the strength of the structure and, if the crack is sufficiently long, the structure will fall below the designed limit load. The assessment of the defect criticality for the structural performance is a major objective of fracture mechanics. Another common situation where fracture mechanics has been found extremely useful is in the prediction of the maximum crack size that can be allowed in a structure.

The field of fracture mechanics traditionally involves applied mechanics and materials science. Applied mechanics relates external loads applied to a flawed, or cracked, structural component to crack-tip stress fields and elastic deformations of the material in the vicinity of the crack tip. Materials

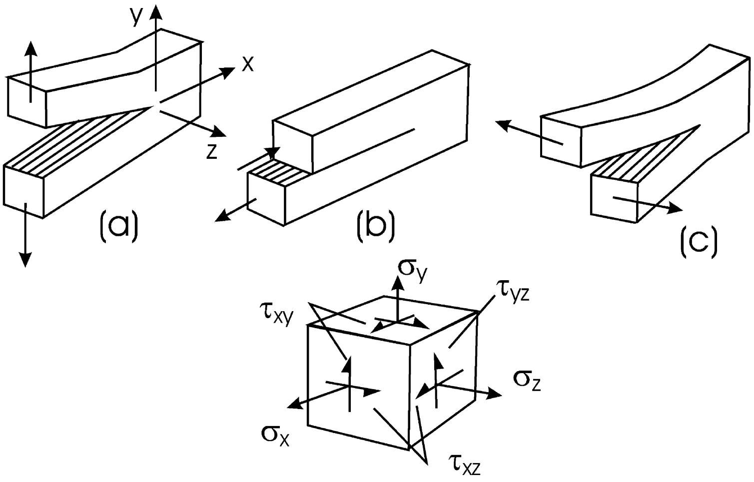

Figure 9.2 Modes of crack loading and definition of stress components: (a) mode I (opening), (b) mode II (forward shear), and (c) mode III (tearing).

science, on the other hand, views fracture mechanics as a means of characterizing the fracture resistance of a material and this understanding will aid in the development of improved processing strategies and materials design.

Most published work on fracture mechanics concerns fracture of isotropic materials such as metals and polymers (Ewalds and Wanhill, 1989; Kinloch and Young, 1983) although there are more recent compilations on fracture mechanics of composites (e.g., Friedrich, 1989; Armanios, 1996). The review article by Hutchinson and Suo (1992) is an excellent source for fracture mechanics of orthotropic and layered dissimilar materials.

Fracture mechanics analysis is most commonly concerned about the opening mode of fracture, i.e. mode I, associated with opening displacements of the crack faces and tensile stresses near the crack tip (see Figure 9.2a). In general, analysis of the forward shear (mode II) and tearing modes (mode III), illustrated in Figures 9.2b and c, is required. Figure 9.2 also shows a commonly used xyz coordinate system and the associated stress element with σ_y, τ_{xy} and τ_{yz}, being the dominant mode I, mode II, and mode III stresses. As discussed by Hutchinson and Suo (1992), an interface crack between two dissimilar materials is inherently loaded in mixed mode because of the mismatch in material properties across the crack interface. This means that both normal and shear stresses act on the interface in front of the crack tip.

We will first consider a true interface crack between a homogeneous, isotropic or orthotropic face sheet and a homogeneous, isotropic core, i.e., the case shown at the far right in Figure 9.1. It is recognized that such a crack constitutes a "bimaterial interface crack" according to the terminology of Suo and Hutchinson (1990). For foam-cored sandwich structures, the combination of stiff faces and a soft core is associated with a tremendous stiffness mismatch. Face-to-core modulus ratios in the range from 100 to 1,000 are common. A bimaterial crack displays some peculiar behavior due to the mismatch in elastic stiffnesses across the crack plane. Mixed mode loading is inherent at the tip of a bimaterial interface crack even if the global load is pure mode I. The asymmetries of moduli and Poisson's ratios across the interface cause mixed mode loading at the crack tip because tensile and shear stresses must appear along the interface to maintain continuity in displacements between the two materials. The stresses near the crack tip experience the typical square root singularity of homogeneous fracture and, in addition, oscillatory behavior (Williams, 1959; England, 1965; Erdogan, 1965; Rice and Sih, 1965). Hutchinson (1990) proposed the following complex representation of the interfacial normal and shear stresses (σ_y and τ_{xy}), see Figure 9.3, ahead of the crack tip ($\theta = 0$):

$$\sigma_y + i\tau_{xy} = \frac{(K_1 + iK_2)x^{i\varepsilon}}{\sqrt{2\pi x}}, \tag{9.1}$$

where x is the distance from the tip along the interface, $i = \sqrt{-1}$, and $K = K_1 + iK_2$ is called "the complex stress intensity factor" for an interfacial crack (Hutchinson, 1990). Notice here that K_1 and K_2 do not represent the opening and sliding modes as K_I and K_{II} do in classical fracture mechanics and no simple physical interpretation of K_1 and K_2 exists. The parameter ε is called the "oscillatory index" (Hutchinson, 1990), defined in terms of one of Dundurs' (1969) elastic mismatch parameters, β,

$$\varepsilon = \frac{1}{2\pi} \ln\left(\frac{1-\beta}{1-\beta}\right), \tag{9.2a}$$

$$\beta = \frac{1}{2}\frac{G_1(1-2\nu_2) - G_2(1-2\nu_1)}{G_1(1-\nu_2) + G_2(1-\nu_1)}, \tag{9.2b}$$

where subscripts 1 and 2 on the shear modulus G and Poisson's ratio ν represent the (isotropic) materials above and below the crack plane. The parameter β vanishes if both materials are identical ($G_1 = G_2$), and when both materials are incompressible ($\nu_1 = \nu_2 = 1/2$).

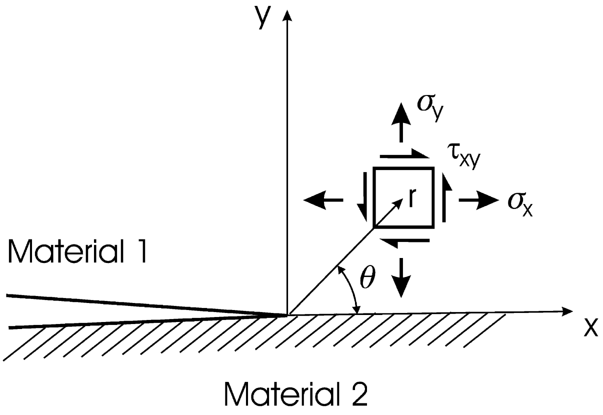

Figure 9.3 Stress element near a bimaterial crack tip.

With $x^{i\varepsilon} = \cos(\varepsilon \ln x) + i \sin(\varepsilon \ln x)$, it is noted that $x^{i\varepsilon}$ in Equation (9.1) is a function that changes sign infinitely often, thus oscillating in a violent manner as the distance x tends to zero. Also, the near tip displacements of the crack face behind the crack tip display oscillatory behavior.

He and Hutchinson (1989) argued that the oscillation is a mathematical artifact of the elasticity solution and showed that the oscillatory region is usually exceedingly small. They proposed a consistent, pragmatic approach to suppress the role of the oscillations by assuming $\varepsilon = 0 = \beta$ both in the evaluation of fracture toughness and in the subsequent application of the toughness data for prediction of crack propagation. For this case, the mode I and mode II stress intensity factors, K_{I} and K_{II}, assume their classical, conventional relation to the opening (σ_y) and shear stresses (τ_{xy}) at the interface ahead of the crack tip ($\theta = 0$).

Suo (1990) examined a crack between two orthotropic solids (or one orthotropic and one isotropic) and determined the near tip stress and displacement fields. For the case where $\varepsilon = \beta = 0$, the following expressions for the stresses and crack flank displacements were derived:

$$\left(\frac{H_{22}}{H_{11}}\right)^{1/2} \sigma_y + i\tau_{xy} = \frac{K_{\mathrm{I}} + iK_{\mathrm{II}}}{\sqrt{2\pi x}}, \tag{9.3a}$$

$$\left(\frac{H_{11}}{H_{22}}\right)^{1/2} \delta_{\mathrm{I}} + i\delta_{\mathrm{II}} = \frac{2H_{11}(K_{\mathrm{I}} + iK_{\mathrm{II}})\sqrt{x}}{\sqrt{2\pi}}, \tag{9.3b}$$

where the stress components are defined in the element shown in Figure 9.3. δ_{I} and δ_{II} are the opening (y directional) and sliding (x directional) displace-

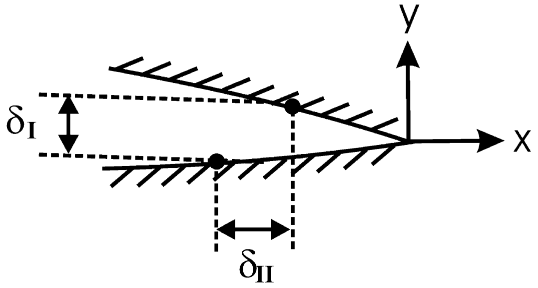

Figure 9.4 Opening (δ_{I}) and sliding (δ_{II}) displacements of the crack surfaces behind the crack tip.

ments of a point located at a distance, x, behind the crack tip before the cracked structure is loaded, see Figure 9.4.

The parameters H_{11} and H_{22} are defined in terms of the orthotropic compliances (b_{ij}) of the materials above and below the crack plane, Figure 9.3,

$$H_{11} = \sum_{i=1}^{2} \left[2n\lambda^{1/4}(b_{11}b_{22})^{1/2}\right]_i, \tag{9.4a}$$

$$H_{22} = \sum_{i=1}^{2} \left[2n\lambda^{-1/4}(b_{11}b_{22})^{1/2}\right]_i, \tag{9.4b}$$

where $i = 1$ for the material above the crack, and $i = 2$ for the material below the crack, and

$$n_i = \left[\frac{1}{2}(1+\rho_i)\right]^{1/2}. \tag{9.5}$$

λ and ρ are defined below in terms of b_{ij}, where the subscripts i, j refer to the material description and assume values of 1, 2, and 6,

$$\lambda = \frac{b_{11}}{b_{22}}, \tag{9.6a}$$

$$\rho = \frac{b_{12} + b_{66}/2}{\sqrt{b_{11}b_{22}}}, \tag{9.6b}$$

$$b_{ij} = \begin{cases} s_{ij} & \text{(plane stress)}, \\ s_{ij} - \dfrac{s_{i3}\, s_{j3}}{s_{33}} & \text{(plane strain)}. \end{cases} \tag{9.6c}$$

s_{ij} ($i, j = 1, 2, 6$) are the compliance elements defined by, e.g., Hyer (1998), for a specially orthotropic material with the 1 direction along the x axis, 2 direction along the y axis, and 3 direction along the z axis.

$$\begin{aligned} s_{11} &= \frac{1}{E_1}, \quad s_{12} = -\frac{\upsilon_{12}}{E_1}, \quad s_{13} = -\frac{\upsilon_{13}}{E_1}, \\ s_{22} &= \frac{1}{E_2}, \quad s_{23} = -\frac{\upsilon_{23}}{E_2}, \quad s_{33} = \frac{1}{E_3}, \\ s_{44} &= \frac{1}{G_{23}}, \quad s_{55} = \frac{1}{G_{13}}, \quad s_{66} = \frac{1}{G_{12}}. \end{aligned} \tag{9.7}$$

Once the stress intensity factors are determined, the energy release rate is obtained according to Suo (1990),

$$G = \frac{H_{11}}{4}[K_{\mathrm{I}}^2 + K_{\mathrm{II}}^2]. \tag{9.8}$$

If both materials above and below the crack plane are isotropic, Equation (9.3a) simplifies to (9.1), and (9.3b) simplifies to

$$\delta_{\mathrm{I}} + i\delta_{\mathrm{II}} = 4\sqrt{\frac{x}{2\pi}}\left(\frac{1}{\bar{E}_1} + \frac{1}{\bar{E}_2}\right)(K_{\mathrm{I}} + iK_{\mathrm{II}}), \tag{9.9}$$

where $\bar{E} = E/(1 - \nu^2)$ for plane strain, where ν is Poisson's ratio, and $\bar{E} = E$ for plane stress. Subscripts 1 and 2 denote the materials above and below the crack plane. For this case the energy release rate, Equation (9.8), becomes

$$G = \frac{1}{2}\left(\frac{1}{\bar{E}_1} + \frac{1}{\bar{E}_2}\right)(K_{\mathrm{I}}^2 + K_{\mathrm{II}}^2). \tag{9.10}$$

If both materials above and below the crack plane are the same, and if they are isotropic, the crack face displacements become

$$\delta + i\delta_{\mathrm{II}} = 8\sqrt{\frac{x}{2\pi}}\frac{(K_{\mathrm{I}} + K_{\mathrm{II}})}{\bar{E}} \tag{9.11}$$

and the energy release rate becomes

$$G = \frac{K_{\mathrm{I}}^2 + K_{\mathrm{II}}^2}{\bar{E}}. \tag{9.12}$$

It should be pointed out that the area of bimaterial fracture mechanics is still emerging. Several approaches, such as the method of distributed dislocations to represent a crack-like discontinuity, have emerged since the pioneering works of Eshelby et al. (1953) and Stroh (1958). Ting (1986) extended this approach to anisotropic materials and Kardomateas and co-workers applied it to bimaterial cracks between dissimilar anisotropic materials (see Huang and Kardomateas, 2001; Liu et al., 2004; Li and Kardomateas, 2006). This last paper also considers crack branching (crack kinking), which is an important failure mode of sandwich structures, see Section 9.2.

9.1.1 Finite Element Crack Closure Method

Several studies of debonding and delamination of composite materials express the crack loading in terms of the energy release rate, G. Since the fracture toughness, G_c, typically depends on the fracture mode, it is common to separate G into "components" corresponding to the opening and shearing modes of fracture, i.e.,

$$G = G_{\mathrm{I}} + G_{\mathrm{II}} + G_{\mathrm{III}}. \tag{9.13}$$

Theoretically, the mode separations is based on Irwin's contention that if the crack extends by a small amount, Δa, the energy absorbed in the process is equal to the work required to close the crack to its original length (Irwin, 1958). This equality is expressed in the following crack closure integrals

$$G_{\mathrm{I}} = \lim_{\Delta a \to 0} \frac{1}{2\Delta a} \int_0^{\Delta a} \sigma_y(\Delta a - r, 0)\bar{v}(r, \pi)dr, \tag{9.14a}$$

$$G_{\mathrm{II}} = \lim_{\Delta a \to 0} \frac{1}{2\Delta a} \int_0^{\Delta a} \tau_{xy}(\Delta a - r, 0)\bar{u}(r, \pi)dr, \tag{9.14b}$$

$$G_{\mathrm{III}} = \lim_{\Delta a \to 0} \frac{1}{2\Delta a} \int_0^{\Delta a} \tau_{yz}(\Delta a - r, 0)\bar{w}(r, \pi)dr, \tag{9.14c}$$

where r is the radial distance from the crack tip, σ_y, τ_{xy}, and τ_{yz} are the normal and shear stresses ahead of the crack tip, and $\bar{v}$, $\bar{u}$ and $\bar{w}$ are the relative opening and sliding displacements between points on the crack faces behind the crack tip.

The mode separation assumes that the crack will extend in a planar fashion, which it may or may not. For mixed mode loading, the crack may tend to deflect (kink) and propagate in a different plane than the original reference plane. This will be discussed in the next section. Furthermore, as pointed out by several authors, if the crack is at a bimaterial interface, the oscillations of stresses and displacements near the crack tip discussed early in this chapter will make the separation of G into components (Equations (9.13) and (9.14)) problematic (Raju et al., 1988).

The crack closure integrals in Equations (9.14) have been implemented into a finite element computation by Rybicki and Kanninen (1977). This method is called "the finite element crack closure method" and has been widely applied to fracture problems, see the review by Kruger (2004). Berggreen (2004) developed a method to extract the stress intensity factors from a finite element solution of the near crack-tip displacements called the

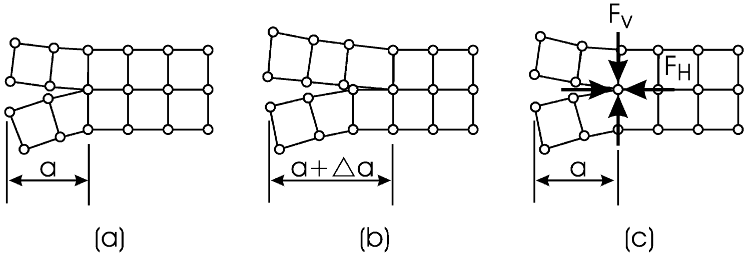

Figure 9.5 The crack-closure technique in finite elements. F_H and F_V are horizontal and vertical forces applied to close the crack. (a) Original configuration, (b) configuration after release of crack-tip nodes, (c) the released nodes are brought back to their initial position by application of nodal forces.

"crack surface displacement extrapolation method". This method has been applied to several bimaterial crack problems.

Figure 9.5 illustrates the crack-closure method applied to a finite-element mesh of a mixed mode I and mode II two-dimensional problem. A certain crack extension Δa may be introduced in the finite-element mesh by releasing duplicate nodes at the crack tip. The resulting deformations are the relative opening and sliding crack-tip deformations. By applying forces to the released nodes in two orthogonal directions, it is possible to close the crack tip to its original state. The products of crack-tip nodal displacements and forces enable G_{I} and G_{II} to be evaluated numerically.

For the plane situation illustrated in Figure 9.5, G_{I} and G_{II} become

$$G_{\mathrm{I}} = \frac{F_V \Delta v}{2b\Delta a}, \tag{9.15a}$$

$$G_{\mathrm{II}} = \frac{F_H \Delta u}{2b\Delta a} \tag{9.15b}$$

where b is the width, F_H and F_V are the horizontal and vertical crack-closure forces, and Δu and Δv are the horizontal and vertical increments of displacements required to bring the released nodes to their original positions. Notice that the far-field load applied is held constant in the steps illustrated in Figure 9.5. For mode III, G_{III} is similarly obtained as

$$G_{\mathrm{III}} = \frac{F_T \Delta w}{2b\Delta a} \tag{9.16}$$

where F_T is the magnitude of the crack-closure forces applied parallel to the crack front and Δw is the z directional incremental displacement required to close the crack.

Implicit in the calculations outlined above is the requirement that the elements enclosing the crack-tip are identical in size. Consequently, Δa is equal to the distance between adjacent nodes. This constraint can be relaxed in case a non-uniform crack tip mesh is used, but the calculations of G_{I}, G_{II} and G_{III} must be modified (see Rybicki and Kanninen, 1977).

It should be observed that the released nodes are assumed to displace in opposite directions with the same magnitude. This is the situation encountered in symmetric crack geometries and specimens. For asymmetric crack geometries and cracks between dissimilar materials, the displacements of the released nodes may no longer be of equal magnitude and the procedure will have to be modified. The basic principle, as for the homogeneous and symmetric case discussed above, is the calculation of the work required to bring the nodes back to their original position, before they were released. For further details on the crack closure method, see, e.g. Kruger (2004).

9.2 Crack Kinking Analysis

If a sandwich structure that contains a face/core debond is loaded, the debond may propagate under certain conditions governed by the crack driving force and the fracture resistance of the material around the tip of the debond. It has been observed that face/core debonds in foam-cored sandwich specimens and panels may propagate at the face/core interface or it may deflect, “kink”, away from the interface and propagate inside the foam core, see Figure 9.6.

Erdogan and Sih (1963) examined crack propagation in a homogeneous, isotropic, brittle plastic sheet. Specifically, a plate containing a central crack of length $2a$ loaded in biaxial tension was analyzed using the Griffith theory assuming the crack will grow in a direction where the energy release per unit crack extension is maximum. They found that the crack growth initiates at the tip and extends in a plane perpendicular to the direction of maximum tangential stress, σ_θ as confirmed by experiments. The near tip stress element in polar coordinates (r, θ) is shown in Figure 9.7.

Following the analysis of Erdogan and Sih (1963), Prasad and Carlsson (1994a) considered a crack of length $2a$ in a homogeneous, isotropic material loaded under plane strain in mixed mode I and mode II. The stresses near the right crack tip, illustrated in Figure 9.7, can be expressed as

$$\sigma_r = \frac{1}{\sqrt{2\pi r}} \cos\frac{\theta}{2}\left(K_I\left(1+\sin^2\frac{\theta}{2}\right)+\frac{3}{2}K_{II}\sin\theta - 2K_{II}\tan\frac{\theta}{2}\right), \tag{9.17a}$$

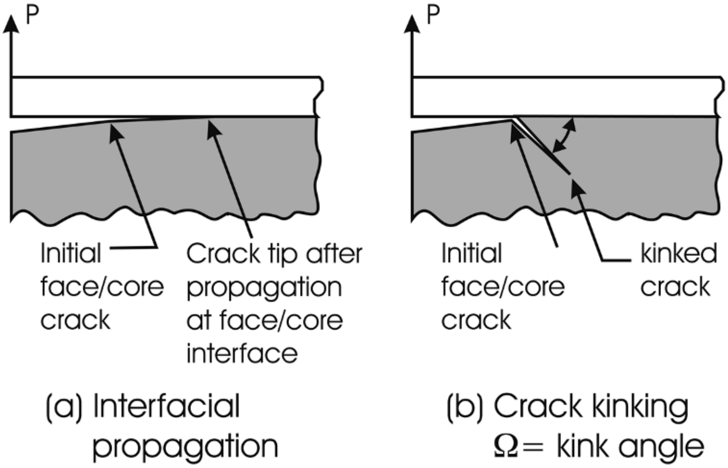

Figure 9.6 Growth scenarios of a face/core debond in foam-cored sandwich.

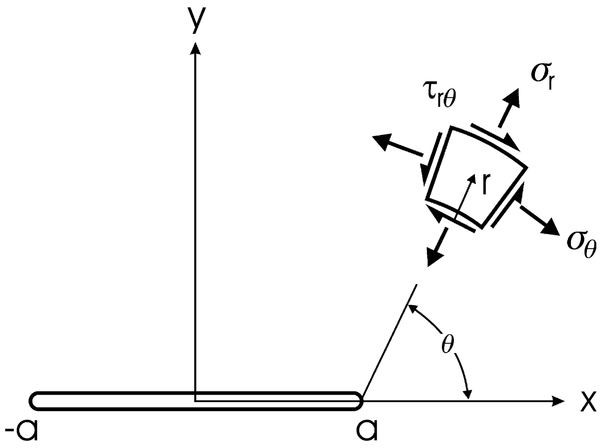

Figure 9.7 Near tip stresses in a cracked sheet.

$$\sigma_\theta = \frac{1}{\sqrt{2\pi r}} \cos\frac{\theta}{2}\left(K_I \cos^2\frac{\theta}{2} - \frac{3}{2}K_{II}\sin\theta\right), \tag{9.17b}$$

$$\tau_{r\theta} = \frac{1}{2\sqrt{2\pi r}} \cos\frac{\theta}{2}\left(K_I \sin\theta + K_{II}\left(3\cos\theta - 1\right)\right). \tag{9.17c}$$

To determine the kink angle, Ω, Figure 9.8, for a general mixed mode loading case, one may determine the direction where the stress σ_θ is maximum. This direction coincides with the direction, $\theta = \Omega$, where the shear stress $\tau_{r\theta}$ vanishes. An explicit expression for Ω was derived by Prasad and

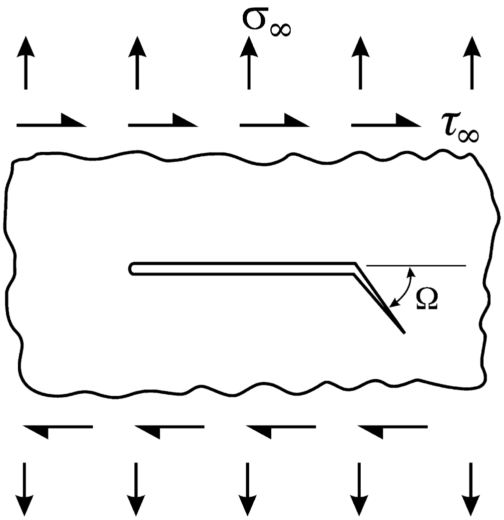

Figure 9.8 Definition of kink angle, Ω, for a crack under mixed mode loading.

Carlsson (1994a) based on Equation (9.17c) with $\tau_{r\theta} = 0$ for $\theta = \Omega$, which yields

$$\frac{\sin\Omega}{3\cos\Omega - 1} = \frac{K_{\mathrm{II}}}{K_{\mathrm{I}}}. \tag{9.18}$$

To solve for the angle Ω in terms of the mode ratio $K_{\mathrm{II}}/K_{\mathrm{I}}$, the following trigonometric identities are employed:

$$\sin^2\frac{\Omega}{2} + \cos^2\frac{\Omega}{2} = 1, \tag{9.19a}$$

$$\cos\Omega = \cos^2\frac{\Omega}{2} - \sin^2\frac{\Omega}{2}, \tag{9.19b}$$

$$\sin\Omega = 2\sin\frac{\Omega}{2} - \cos\frac{\Omega}{2}. \tag{9.19c}$$

Substitution of Equations (9.19) in (9.18) yields

$$\frac{\sin\frac{\Omega}{2}\cos\frac{\Omega}{2}}{\cos^2\frac{\Omega}{2} - 2\sin^2\frac{\Omega}{2}} = \frac{K_{\mathrm{II}}}{K_{\mathrm{I}}}. \tag{9.20}$$

After factoring out $\cos^2(\Omega/2)$, this equation simplifies to

$$\frac{\tan\frac{\Omega}{2}}{1 - 2\tan^2\frac{\Omega}{2}} = \frac{K_{\mathrm{II}}}{K_{\mathrm{I}}}. \tag{9.21}$$

Substitution of $x = \tan(\Omega/2)$ into Equation (9.21) yields

$$2K_{\mathrm{II}}x^2 + K_{\mathrm{I}}x = K_{\mathrm{II}}. \tag{9.22}$$

Solving the quadratic yields

$$\tan\frac{\Omega}{2} = \frac{-1 \pm \sqrt{1 + 8(K_{\mathrm{II}}/K_{\mathrm{I}})^2}}{4(K_{\mathrm{II}}/K_{\mathrm{I}})}. \tag{9.23}$$

Hence, the kink angle may be expressed as

$$\Omega = 2\tan^{-1}\left[\frac{-1 \pm \sqrt{1 + 8(K_{\mathrm{II}}/K_{\mathrm{I}})^2}}{4K_{\mathrm{II}}/K_{\mathrm{I}}}\right]. \tag{9.24}$$

Pure mode I, $K_{\mathrm{II}} = 0$, yields a kink angle, $\Omega = 0$, i.e., self-similar propagation, while pure mode II yields $\Omega = \pm 70.5°$, where the + sign refers to kinking down as shown in Figure 9.8 ($K_{\mathrm{II}} > 0$) and the − sign refers to kinking up ($K_{\mathrm{II}} < 0$).

This analysis thus provides the direction of kinking if it were to occur in a homogeneous and isotropic material. The initiation of the kinked crack growth occurs under mixed mode conditions and the fracture toughness, K_c, may depend upon the amount of mode II present, i.e., the mode ratio $K_{\mathrm{II}}/K_{\mathrm{I}}$. Hence, for a given material, it is necessary to experimentally measure the fracture toughness at various mode mixes. Experimentally it has been found that the fracture toughness increases with increased shear loading (increasing mode ratio, $K_{\mathrm{II}}/K_{\mathrm{I}}$) (Liechti and Chai, 1992).

For a face/core crack, the various growth scenarios illustrated in Figure 9.1 point to one possibility that the initial debond lies between two widely dissimilar material, i.e. between a stiff face and a compliant (soft) core. Crack kinking for such a case has been examined by He and Hutchinson (1989) who considered a crack at the interface between two dissimilar isotropic materials, #1 above the interface, and #2 below the interface. A straight crack segment denoted "kinked crack" in Figure 9.6b, of short length compared to the "parent", interface crack (Figure 9.6a) was specifically analyzed. The stress field prior to kinking is thus the singularity field of an interface crack which corresponds to a strain energy release rate, G, available for further propagation along the interface or kinking into the core. The analysis provides the energy release rate of the kinked crack, G^k, using an extensive numerical solution of the governing integral equations. The energy release rate and kink angle results are presented graphically for any given combinations of materials above and below the interface specified in terms of an elastic mismatch parameter α (Dundurs, 1969),

$$\alpha = \frac{\overline{E_1} - \overline{E_2}}{\overline{E_1} + \overline{E_2}}, \tag{9.25}$$

where $\overline{E} = E$ for plane stress, and $\overline{E} = E/(1 - \upsilon^2)$ for plane strain. Subscripts 1 and 2 on Young's modulus represents the materials above and below the crack plane.

He and Hutchinson (1989) examined the energy release rate ratio G^k/G and found that this ratio increases with increasing compliance of the material into which the crack kinks. They suggested that the crack would remain at the interface only if the compliant material is tough and the interface is relatively brittle. Furthermore, as discussed by Hutchinson and Suo (1992), the kink angle that maximizes, G^k, is also the angle where $K_{\mathrm{II}} = 0$, i.e., the kinked crack propagates under pure mode I as for the homogeneous case discussed earlier. The considerations discussed above were expressed in an energy inequality governing kinking,

$$\frac{G^k_{\max}}{G} > \frac{G_{IC}}{G_C}, \tag{9.26}$$

where $G^k_{\max}$ is the maximum energy release rate for the kinked crack with respect to kink angle, Ω and G is the energy release rate of the interface crack. G_{IC} and G_C are the mode I fracture toughness of the core, and the interface fracture toughness, respectively.

Predictions of the crack propagation path in a sandwich panel according to the above analysis thus requires experimental data on the core fracture toughness, G_{IC}, and the interface toughness, G_C, at the mixed mode loading (K_{I}, K_{II}) acting on the tip of the interface crack. Measurement of G_{IC} for the core is quite straightforward, but the measurement of the interface toughness, G_C, is more difficult, unless G_c is low and the crack propagates at the interface. If the interface is much tougher than the core, however, experimental determination of G_C becomes very difficult since the crack would not select such a high resistance path. Without a value of G_C the analysis could still be used in a semi-quantitative sense providing the direction Ω of the kinked crack and the driving force for kinking indicated by the energy release ratio $G^k_{\max}/G$.

9.2.1 Crack Path in Foam-Cored DCB Specimens

Understanding of the factors that govern the crack path in foam-cored sandwich structures is essential for the design of such structures. Furthermore,

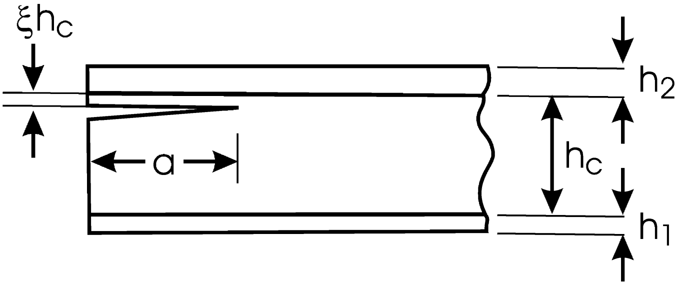

Figure 9.9 Precrack in a foam core DCB specimen. ξ is a parameter specifying the location of the precrack below the upper face in the core ($0 \leq \xi \leq 1$).

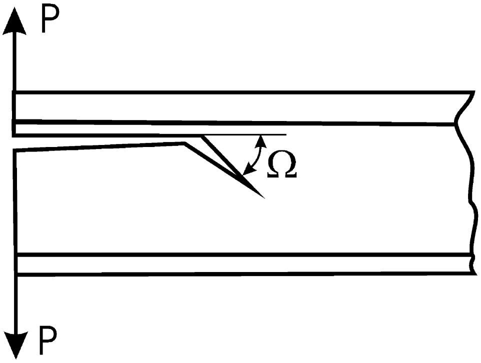

Figure 9.10 Crack kinking in foam-cored sandwich DCB specimen. Positive kink angle Ω is defined as shown ("down").

measurement of face/core debond toughness requires that the crack remains at the face/core interface. It has been found that kinking of the crack into the core is a common occurrence in DCB testing of foam-cored sandwich specimens (see Prasad and Carlsson, 1994b). Kinking would disqualify the test data for interface toughness.

When a foam core sandwich DCB specimen is tested, it is common to slightly extend the precrack beyond the tip of the artificial film insert at the face/core interface and this may tend to bring the precrack into the core below the face/core interface, as shown in Figure 9.9. If the DCB specimen is prepared from a sandwich panel without a starter film, the precrack needs to be cut into the core, near the face/core interface, which also tends to produce a precrack such as the one illustrated in Figure 9.9.

As discussed in Section 9.2, a crack in a foam-cored DCB specimen may not propagate in a self-similar manner, but kink up or down in a certain direction quantified by the kink angle Ω (Figure 9.10). The direction of kinking

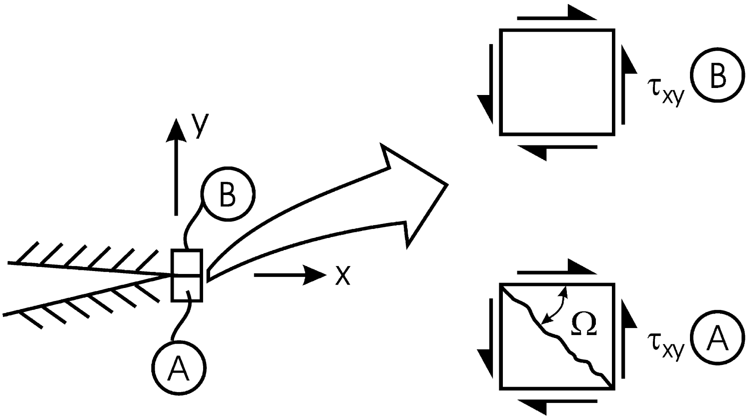

Figure 9.11 Positive shear stress and kink angle.

is indicated by the sign of the angle Ω ($\Omega > 0$ in Figure 9.10). The positive sign of the kink angle in Figure 9.10 is consistent with a positive shear stress ahead of the crack tip, see Figure 9.11. Furthermore, a positive shear stress ahead of the crack tip is consistent with the direction of sliding of the crack faces behind the crack tip, as shown in Figure 9.4.

Analysis of the kinking angle and critical load required to initiate kinking of a crack (Section 9.2) requires the stress intensity factors and energy release rate at the front of the parent crack. Such analysis, however, requires substantial detail since the definition of stress intensity factors is based on stresses and displacements in a very small region (singular domain) near the crack tip.

As a simpler alternative to detailed fracture mechanics is the beam theory analysis presented by Carlsson et al. (2006). If the influence of the small singular field domain near the crack tip is neglected, it is possible to determine the relative sliding displacement, shown in Figure 9.4, from the bending strains

$$\delta_{ii} = r(\varepsilon_x^L - \varepsilon_x^U), \tag{9.27}$$

where ε_x represents the near crack tip bending strains in the crack flanks, superscripts L and U denote the lower (L) and upper (U) sub-beams (legs), and r is the distance from the crack tip. According to this analysis, kinking would be promoted by a bending strain mismatch between the lower and upper legs of the DCB sandwich specimen, i.e. $\delta_{\mathrm{II}} \neq 0$ in Equation (9.26). $\delta_{\mathrm{II}} > 0$ would promote kinking downwards and $\delta_{\mathrm{II}} < 0$ would promote kinking upwards. Zero difference would promote self-similar growth (if the initial crack is within the core).

To quantify the strain mismatch, a DCB specimen with the generic crack configuration shown in Figure 9.9 is considered. The crack is located at distance ξh_c from the upper face/core (F/C) interface and a distance $(1-\xi)h_c$ from the lower F/C interface, where h_c is the core thickness and the parameter ξ is bounded by $0 \leq \xi \leq 1$. Consequently, $\xi = 0$ corresponds to a crack at the upper F/C interface, and $\xi = 1$ represents a crack at the lower F/C interface. The face sheets may have different moduli (E_{f1} and E_{f2}) and thicknesses (h_1 and h_2). We will here assume that each face sheet can be considered as homogeneous isotropic or orthotropic and the core is isotropic. The bending of each leg of the DCB is modeled using a laminated beam formulation where the extensional, coupling, and bending stiffness matrices of classical laminated plate theory, i.e. $[A]$, $[B]$ and $[D]$ as defined in Equations (3.18) and (3.19), are replaced by three scalar stiffnesses, A, B and D given by

$$A = \sum_{k=1}^{N} (E_x)_k (z_k - z_{k-1}), \tag{9.28a}$$

$$B = \frac{1}{2}\sum_{k=1}^{N} (E_x)_k (z_k^3 - z_{k-1}^3), \tag{9.28b}$$

$$D = \frac{1}{3}\sum_{k=1}^{N} (E_x)_k (z_k^3 - z_{k-1}^3), \tag{9.28c}$$

where the ply coordinates z_k are defined for a general laminate in Figure 3.2.

Application of this analysis to the bending of the lower and upper legs of the DCB specimen shown in Figure 9.9, each subject to a load P, yields the strains ε_x^L and ε_x^U as required for Equation (9.27).

$$\frac{\varepsilon_x^L b}{Pa} = \frac{h_L/2 - B_L/A_L}{D_L - B_L^2/A_L} \quad \text{(lower)}, \tag{9.29a}$$

$$\frac{\varepsilon_x^U b}{Pa} = \frac{h_U/2 + B_U/A_U}{D_U - B_U^2/A_U} \quad \text{(upper)}, \tag{9.29b}$$

where h_L and h_U are the thicknesses of the lower and upper legs,

$$h_L = h_1 + (1-\xi)h_c, \tag{9.30a}$$

$$h_U = h_2 + \xi h_c. \tag{9.30b}$$

The extensional, coupling, and bending stiffness of the lower and upper legs are obtained from Equations (9.28),

$$A_L = E_{f1}h_1 + E_c(1-\xi)h_c, \tag{9.31a}$$

$$A_U = E_{f2}h_2 + E_c\xi h_c, \tag{9.31b}$$

$$B_L = \frac{h_1h_c(1-\xi)}{2}(E_c - E_{f1}), \tag{9.31c}$$

$$B_U = \frac{\xi h_2h_c(1-\xi)}{2}(E_{f2} - E_c), \tag{9.31d}$$

$$D_L = \frac{1}{12}[E_{f1}(h_1^3 + 3h_1h_c^2(1-\xi)^2) + E_c((1-\xi)^3h_c^3 + 3h_1^2h_c(1-\xi))], \tag{9.31e}$$

$$D_U = \frac{1}{12}[E_c(\xi^3h_c^3 + 3\xi h_ch_c^2) + E_{f2}(h_2^3 + 3\xi^2h_c^2h_c)], \tag{9.31f}$$

where E_{f1} and E_{f2} are the effective Young's moduli of the lower and upper face sheets, respectively, and E_c is the core modulus.

An example (Carlsson et al., 2006) is a symmetric DCB specimen consisting of 2.4 mm thick glass/vinylester faces and a 16 mm thick H100 PVC foam core. The face and core moduli are $E_{f1} = E_{f2} = 27.6$ GPa and $E_c = 105$ MPa. The crack tip strains in the lower and upper legs of the DCB specimen were calculated from Equations (9.29) as a function of the crack position in the core ($0 \leq \xi \leq 1$). Figure 9.12 shows the crack tip strains in the upper and lower legs vs. ξ. The graph shows that the strains are equal ($\delta_{\text{II}} = 0$) at three locations of the crack, i.e., $\xi = 0.08$, 0.5, and 0.92. Consequently, a crack located at these locations is expected to propagate in a self-similar manner. Further, according to this analysis, a crack located at the top interface ($\xi = 0$), would kink down ($\varepsilon_x^L > \varepsilon_x^U$) until it reaches an equilibrium location where the strains are equal ($\xi = 0.08$). This is a stable location since Figure 9.13 indicates that any small perturbation of the crack location (up or down) would tend to return the crack to the $\xi = 0.08$ location. Similarly, a crack at the lower F/C interface ($\xi = 1$) would kink up ($\varepsilon_x^L > \varepsilon_x^U$) until a stable position is reached at $\xi = 0.92$. The actual distance from the upper and lower interface to the stable locations is only about 1.3 mm for this specimen, and a crack propagating at this location would be considered as "near interface". A crack positioned in the upper half region of the core between $\xi = 0.08$ and 0.5 would kink up and approach the $\xi = 0.08$ location while a crack located in the lower half would kink down. A center crack ($\xi = 0.5$) would potentially remain at the center, but Figure 9.12 indicates that this configuration is not stable since any small disturbance (up or down) would promote kinking up or down towards the stable $\xi = 0.08$ or 0.92 locations.

Several other cases were examined by Carlsson et al. (2006).

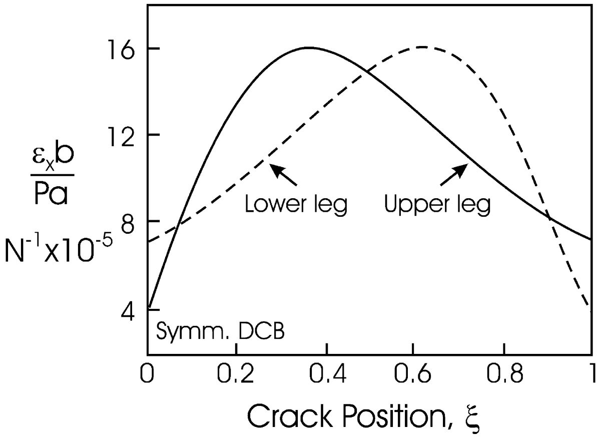

Figure 9.12 Crack tip strains in lower and upper legs of a symmetric DCB specimen.

9.3 Cohesive Zone Models of Face/Core Interface Failure

Producers of sandwich structures sometimes add a mat of continuous fibers called a "continuous filament mat" (CFM), or a "chopped strand mat" (CSM), between the face and core. The purpose of such a design is to increase the resin content between face and core to avoid "dry spots" and improve the resistance to face/core debonding by the increased resin content. The CFM and CSM may also add an additional toughening mechanism provided by fiber bridging the crack surfaces, see the photograph in Figure 9.13 showing face/core separation in a sandwich beam with a CSM added between face and core evidencing large-scale fiber bridging.

In cases where bridging zones develop, the actual material separation displacements across the crack faces can be quite substantial and the large-scale fracture process zone makes linear elastic fracture mechanics concepts difficult to satisfy. In many cases, the global response of a cracked sandwich structure, or fracture test specimen, remains linear, while the material separation process near the crack tip behaves nonlinear. This situation is conveniently represented by a cohesive zone model, where the tensile strength and the work of fracture become connected using a specific traction/separation (T/S) law (Argon, 2000). Figure 9.14 shows an idealized T/S law. As shown, the crack will start to open when the crack tip stress exceeds the cohesive strength σ_0. Once the crack opens up, the cohesion of the material elements

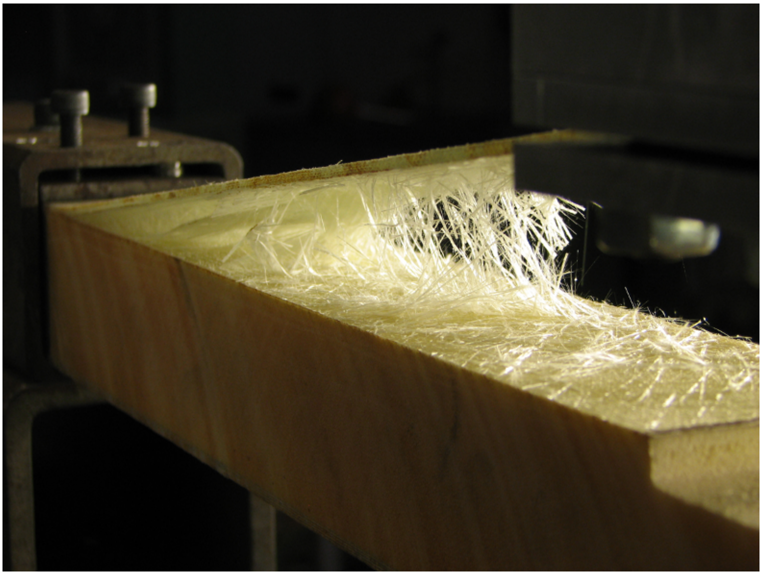

Figure 9.13 Fiber bridging observed during face/core separation in a sandwich beam with a 450 g/m^2 CSM. (Courtesy of Lundsgaard et al., 2008)

behind the crack tip will not be totally lost, as in linear elastic fracture mechanics, until the crack opening exceeds the critical value u_n^c.

As discussed by Nairn (2009) and shown in Figure 9.15, a cohesive zone is associated with two crack tips, viz. the notch root where the traction is zero and the actual crack tip where the material separation is initiated (see Figure 9.15). At the beginning of the fracture process, the bridging zone develops by extension of the crack tip while the notch root remains fixed. As will be discussed below, this process is associated with a rising resistance curve (R curve). After further loading, if a steady-state is reached, the crack tip and notch root propagate at the same rate, corresponding to a constant length of the bridging zone and self-similar growth.

Figure 9.15 also illustrates the separation of the crack flanks at the notch root, u_n^* where the traction vanishes. The fracture process in a test specimen or structure occurs in a "process zone" defining a layer of total thickness, Δ. The process zone is comprised of parts of the face and core materials above and below the interface where fiber pull-out, plastic deformation, and other complex, nonlinear material separation processes occur, see Figure 9.15. In modeling of cohesive failure of fracture test specimens, the local response of the material separation law typically demands a numerical finite element solution with special cohesive elements where the T/S law is specified and

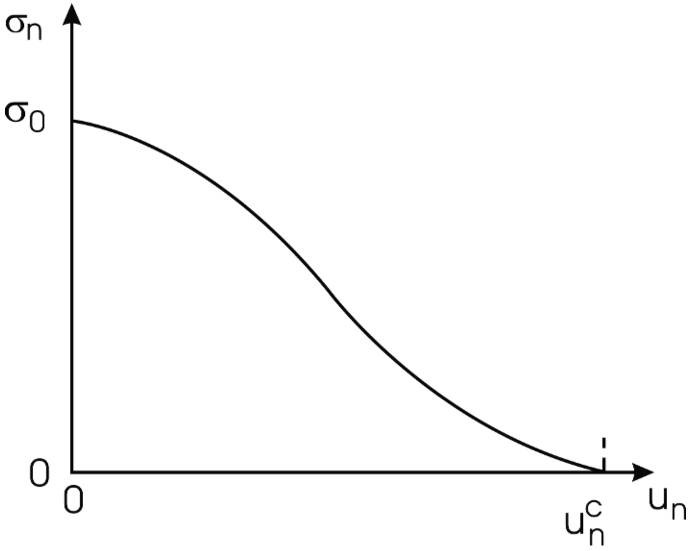

Figure 9.14 Schematic representation of a traction/separation law representing the failure process.

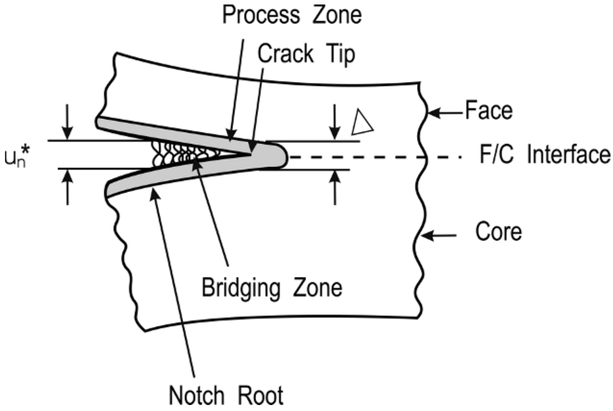

Figure 9.15 Process zone around the crack tip.

assigned along the anticipated crack propagation path, which, for a sandwich structure, is commonly along the face/core interface (Ostergaard, 2007). The layer thickness, Δ, of the process zone is typically neglected.

An important tool in cohesive zone modeling is the J integral proposed by Rice (1968).

$$J = \int_{\Gamma} \left(\Phi \, dx_2 - \sigma_{ij} n_j \frac{\partial u_i}{\partial x_i} ds \right), \tag{9.32}$$

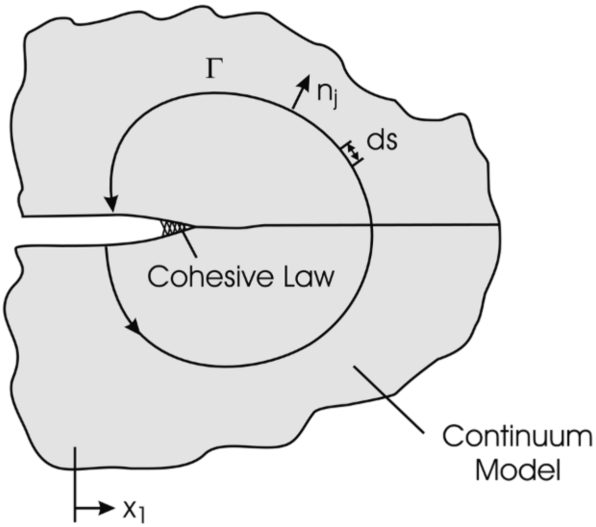

Figure 9.16 Path Γ for calculation of the J integral with normal n_j. x_1 is a coordinate along the crack propagation path and x_2 is perpendicular to the crack plane.

where Γ is any counter-clockwise path surrounding the crack faces, with n_j being the outwards directed normal vector to the path, Γ, see Figure 9.16. x_1 is a coordinate along the crack plane, and u_i is the displacement vector and ds is an element of Γ.

Φ is the strain energy density given by

$$\Phi = \int_0^{\varepsilon} \sigma_{ij} d\varepsilon_{ij}, \tag{9.33}$$

where σ_{ij} and ε_{ij} are i, j elements of the stress and strain tensors, respectively, and repetition of an index denotes summation over the range $i, j = 1, 2, 3$.

For the pure normal opening loading considered here, a cohesive law (Figure 9.14) can be expressed as

$$\sigma_n = \sigma_n(u_n). \tag{9.34}$$

When the stress on the interface reaches its ultimate value, σ_0, the fracture process is initiated. Before that, all deformation of the specimen is accommodated by the continuum. Figure 9.17 schematically illustrates the distribution of normal stress acting in the cohesive zone.

Evaluation of the J integral around the cohesive zone (Li and Ward, 1987; Bao and Suo, 1992) provides the relation between the cohesive law and the

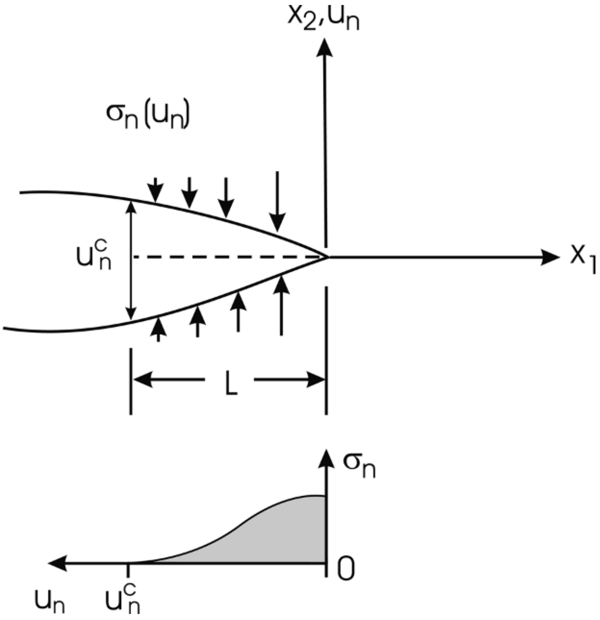

Figure 9.17 Normal stress, σ_n, in the cohesive zone.

fracture resistance:

$$J_r = \int_0^{u_n^*} \sigma_n du_n + J_0, \tag{9.35}$$

where u_n^* is the maximum separation distance encountered at any specific crack length (Figure 9.18). As shown in Figure 9.18, at the beginning of the fracture test no fibers are bridging the crack and the crack will advance when $J_R = J_0$. Upon further loading and extension of the crack tip (Figure 9.18), the first term in Equation (9.35) will start to contribute as a result of development of the bridging zone.

As the crack propagates further, the bridging zone will become more and more developed and extend behind the crack tip corresponding to a rising R curve, i.e., a plot of J_R vs. Δa, where Δa is the extension of the crack tip from its initial value (a_0), see Figure 9.19. Once the maximum end opening, u_n, reaches its critical value, u_n^c, the bridging zone is fully developed, corresponding to a steady-state fracture toughness, $J_R = J_{ss}$. Nairn (2009) has argued that the energy stored in the bridging fibers may be recovered upon unloading the specimen and that a true R curve determination prior to steady-state should subtract this contribution to the J integral. However, this should not be an issue for continuous loading considered here.

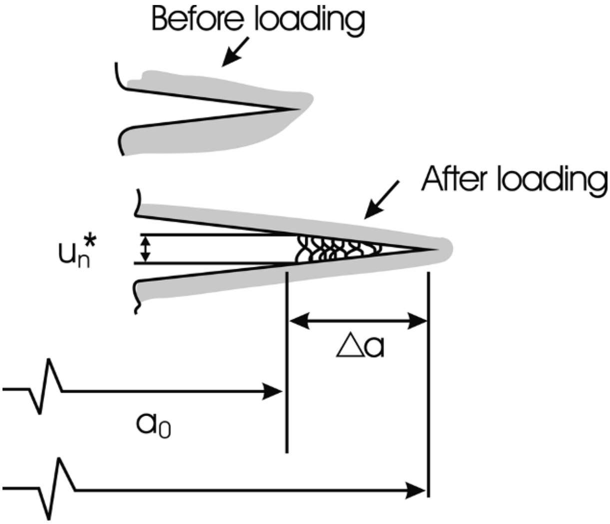

Figure 9.18 Extension of crack tip and development of bridging zone.

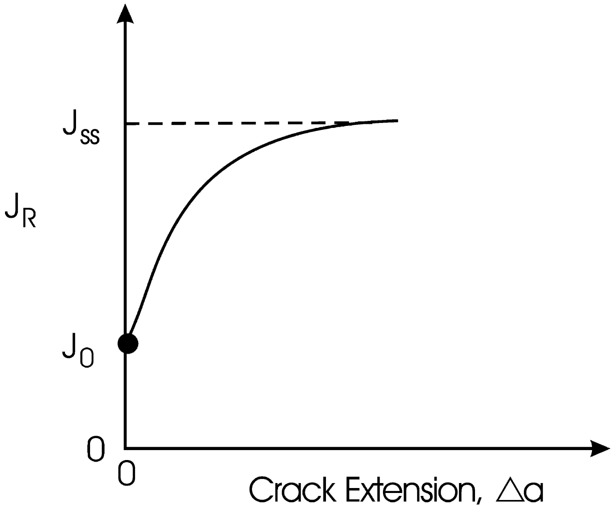

Figure 9.19 Schematic R curve showing crack growth resistance, J_R, vs. crack extension in a material where fiber bridging develops.

As discussed by Ostlund (1995) and Sorensen and Jacobsen (1998), the bridging fibers represent distributed discrete forces, here smeared into a continuum mechanics cohesive stress, σ_n. Such an approach is assumed appropriate if there is a sufficient number of bridging fibers per unit area.

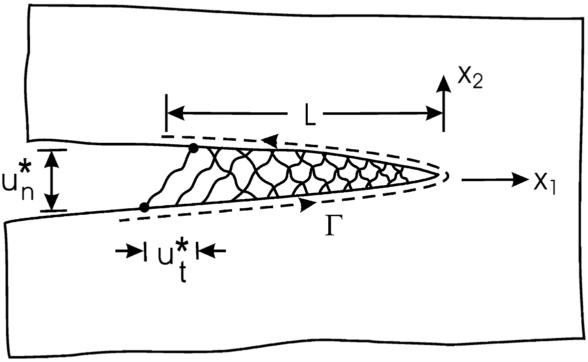

Figure 9.20 Crack with large scale bridging subject to mixed mode loading. After Sorensen and Kirkegaard (2006).

The cohesive law, $\sigma_n = \sigma_n(u_n)$, may be determined from the measured resistance curve. Differentiation of Equation (9.35) yields (Li and Ward, 1989)

$$\sigma_n(u_n) = \frac{dJ_R}{du_n}. \tag{9.36}$$

Such an approach requires that J_R has been determined as a function of the end opening, u_n^*. Hence, the test must employ special displacement measuring devices that allow recording of u_n^* (Lundsgaard et al., 2008).

So far the description has been limited to mode I fracture. The treatment of mixed mode fracture using a cohesive law approach requires consideration of both normal and shear stresses σ_n and τ_{nt} that act in the cohesive zone, and normal and tangential crack face displacements, u_n and u_t. Sorensen and Kirkegaard (2006) present a consistent approach to establish mixed mode cohesive laws for specimens displaying large-scale bridging. The approach utilizes the J integral applied to the novel test method consisting of a DCB specimen (Section 11.7) where the legs are loaded with edge couples as opposed to shear forces in the traditional, standard DCB test. The normal and shear traction/separation stresses are extracted from the J integral in combination with measured normal and tangential crack face displacements at the end of the cohesive zone. Figure 9.20 illustrates the crack region with a large-scale bridging zone subject to mixed mode loading.

The crack opening and sliding displacements u_n and u_t are defined as the relative displacements of the upper and lower crack surfaces (Figure 9.20). The critical values of u_n and u_t are denoted u_n^c and u_t^c. The normal and shear stresses acting over the cohesive zone are denoted by σ_n and τ_{nt}. Calculation of the J integral for a path, Γ (Figure 9.16) starting and ending outside the bridging zone, along the lower crack face, around the crack tip and back along the upper crack face, yields the result

$$J_R = \int_0^{u_n^*} \sigma_n \left(u_n, u_t\right) du_n + \int_0^{u_t^*} \tau_{nt} \left(u_n, u_t\right) du_t + J_0. \tag{9.37}$$

By partially differentiating Equation (9.37) with respect to u_n and u_t, the cohesive stresses become

$$\sigma_n = \frac{\partial J_R}{\partial u_n}, \tag{9.38a}$$

$$\tau_{nt} = \frac{\partial J_R}{\partial u_\tau}. \tag{9.38b}$$

Hence, in this manner the cohesive stresses, i.e. traction/separation (T/S) law, can be determined directly from the measured resistance curve and measured values of the opening and sliding displacements. At steady-state crack propagation, the bridging zone is fully developed and should translate similarly with the growing crack along the interface.

9.4 An Expression for the Energy Release Rate of Face/Core Debonds in Sandwich Beams

A loading which can be especially detrimental for a sandwich structure is compression because these debonds are susceptible to buckling and subsequent rapid growth during the post-buckling phase. Typically, post-buckling solutions are derived in terms of forces and moments at the debond section (Kardomateas and Huang, 2003). Therefore, expressions for the energy release rate in terms of these quantities are particularly useful. Such expressions were first derived by Yin and Wang (1984) for delaminated monolithic composites, and extended by Suo and Hutchinson (1990) to a delaminated bi-material (thin film on a substrate). The sandwich configuration is, however, a “tri-material”, i.e. two face sheets, which need not be the same, and a core. This is the configuration treated in this section. Specifically, we use the J integral to obtain a closed form algebraic expression for the energy release rate, G, for a debonded sandwich beam. The most general case of an “asymmetric” sandwich is considered, i.e. the bottom face sheet is not necessarily of the same material and thickness as the top face sheet. The expression derived is in terms of forces and moments (which are typical outputs of post-buckling solutions) acting on the debonded section.

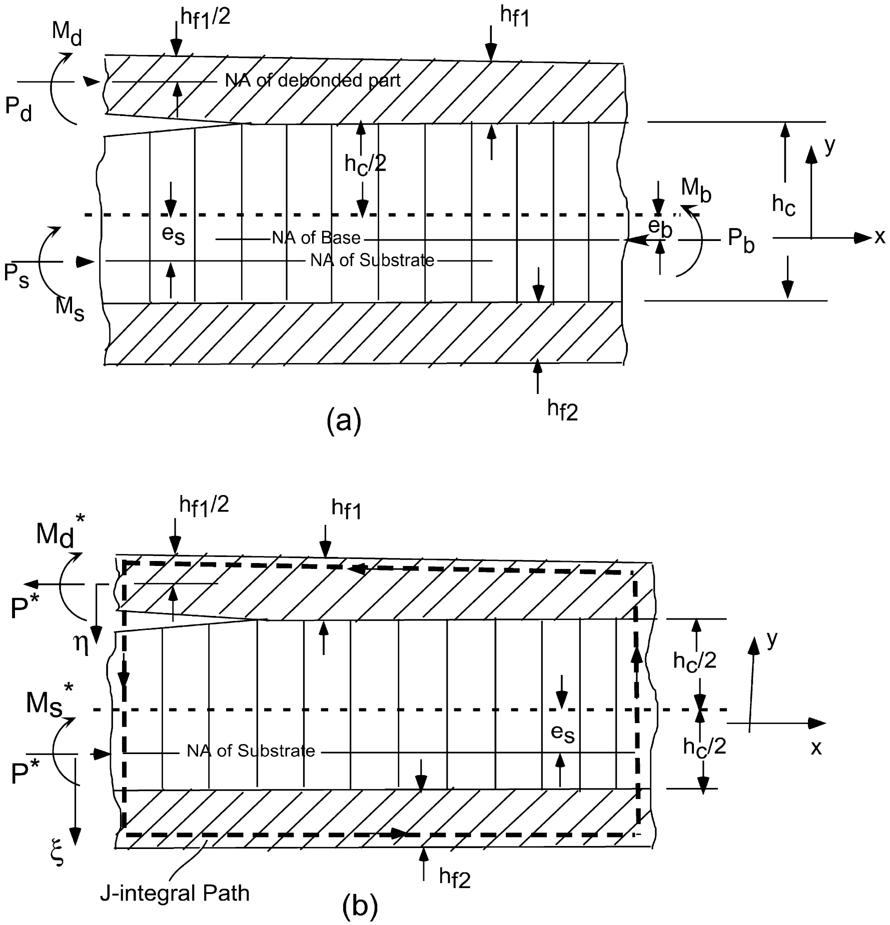

Figure 9.21 (a) Sandwich cross-section with the acting forces and moments; (b) the *J* integral path.

We consider a sandwich beam consisting of two face sheets of thicknesses h_{f1} and h_{f2}, and extensional moduli E_{f1} and E_{f2}, respectively. The core, of thickness h_c, has an extensional modulus, E_c (Figure 9.21a).

In the region of the debond, the sandwich beam consists of two parts: the debonded upper face sheet (referred to as the "debonded part", of thickness h_{f1}) and the part below the debond ("substrate part", of thickness $h_c + h_{f2}$, which includes the core and the lower face sheet). A unit width is assumed. The region outside the debond is referred to as the "base part" and consists of the entire section of the sandwich beam, i.e., of thickness $h_{f1} + h_c + h_{f2}$.

We shall denote the base part with “b”, the debonded part with “d”, and the substrate part with “s”.

A characteristic of sandwich construction is that the neutral axis for the base and the substrate parts is in general no longer at the center of the corresponding sections. With respect to a reference axis x through the middle of the core, the neutral axis of the base section is defined at a distance e_b (Figure 9.21a), as:

$$\begin{aligned} & e_b \left(E_{f1} h_{f1} + E_c h_c + E_{f2} h_{f2} \right) \\ & \quad = E_{f2} h_{f2} \left(\frac{h_{f2}}{2} + \frac{h_c}{2} \right) - E_{f1} h_{f1} \left(\frac{h_{f1}}{2} + \frac{h_c}{2} \right), \end{aligned} \tag{9.39a}$$

and that of the substrate part is at a distance e_s, given by

$$e_s \left[E_c h_c + E_{f2} h_{f2} \right] = E_{f2} h_{f2} \left(\frac{h_{f2}}{2} + \frac{h_c}{2} \right). \tag{9.39b}$$

Moreover, while for the debonded face, which is homogeneous, the bending rigidity per unit width is

$$D_d = E_{f1} \frac{h_{f1}^3}{12}. \tag{9.40a}$$

For the base part the equivalent flexural rigidity of the sandwich section per unit width is (Figure 9.21a)

$$\begin{aligned} D_b = {} & E_{f1} \frac{h_{f1}^3}{12} + E_{f1} h_{f1} \left(\frac{h_{f1}}{2} + \frac{h_c}{2} + e_b \right)^2 + E_{f2} \frac{h_{f2}^3}{12} \\ & + E_{f2} h_{f2} \left(\frac{h_{f2}}{2} + \frac{h_c}{2} - e_b \right)^2 + E_c \frac{h_c^3}{12} + E_c h_c e_b^2, \end{aligned} \tag{9.40b}$$

and for the substrate (again, per unit width)

$$D_s = E_c \frac{h_c^3}{12} + E_c h_c e_s^2 + E_{f2} \frac{h_{f2}^3}{12} + E_{f2} h_{f2} \left(\frac{h_{f2}}{2} + \frac{h_c}{2} - e_s \right)^2. \tag{9.40c}$$

Figure 9.21a shows a segment of the plate containing the debond front (crack tip). A section of the plate ahead of the crack tip carries the compressive axial force P_b and bending moment M_b, per unit width of the plate (base part loads).

Behind the crack tip, the cross-section above the debond (debonded part) carries the loads P_d and M_d and the cross-section below the debond (substrate part) carries the loads P_s and M_s. It is assumed that these forces and moments have already been determined from the post-buckling solution of the plate. It should be noted that in this derivation we consider only the effects of the axial forces and bending moments; shear forces are neglected. In addition, force and moment (about the neutral axis of the base part) equilibrium conditions hold as follows:

$$P_b = P_d + P_s, \tag{9.40d}$$

$$M_b - M_d - M_s - P_d\left(\frac{h_{f1}}{2} + \frac{h_c}{2} + e_b\right) + P_s(e_s - e_b) = 0. \tag{9.40e}$$

If we set

$$(EA)_b = E_{f1}h_{f1} + E_c h_c + E_{f2}h_{f2}, \tag{9.41a}$$

then the axial stress in the base part is

$$\sigma_{xx}^{(b)} = \begin{cases} -\dfrac{P_b}{(EA)_b}E_{f1} - \dfrac{M_b E_{f1}}{D_b}y & \text{if } e_b + \dfrac{h_c}{2} \le y \le e_b + \dfrac{h_c}{2} + h_{f1} \\ & \quad \text{[debonded face]}, \\ -\dfrac{P_b}{(EA)_b}E_c - \dfrac{M_b E_c}{D_b}y & \text{if } e_b - \dfrac{h_c}{2} \le y \le e_b + \dfrac{h_c}{2} \\ & \quad \text{[core]}, \\ -\dfrac{P_b}{(EA)_b}E_{f2} - \dfrac{M_b E_{f2}}{D_b}y & \text{if } e_b - \dfrac{h_c}{2} - h_{f2} \le y \le e_b - \dfrac{h_c}{2} \\ & \quad \text{[lower face]}. \end{cases} \tag{9.41b}$$

Superimposing $-\sigma_{xx}^{(b)}$ on the stresses behind and ahead of the debond front in the system in Figure 9.21a, would result in the system in Figure 9.21b, whose energy release rate and stress intensity factors would be the same as in the original system (Figure 9.21a) since the system of base part stresses acting alone would produce a non-singular stress field. In this way, we can express the energy release rate in just two parameters.

The forces acting on the system in Figure 9.21b are

$$P^* = \int_{e_b+\frac{h_c}{2}}^{e_b+\frac{h_c}{2}+h_{f1}} (-\sigma_{xx}^{(b)})dy - P_d. \tag{9.42a}$$

Substituting $\sigma_{xx}^{(b)}$ from (9.41b) and performing the integration results in P^* in the form

$$P^* = C_1 P_b + C_2 M_b - P_d, \tag{9.42b}$$

where

$$C_1 = \frac{E_{f1}h_{f1}}{(EA)_b}; \quad C_2 = \frac{E_{f1}h_{f1}}{2D_b}(2e_b + h_{f1} + h_c). \tag{9.42c}$$

Likewise,

$$M_d^* = M_d - \int_{e_b+\frac{h_c}{2}}^{e_b+\frac{h_c}{2}+h_{f1}} (-\sigma_{xx}^{(b)}) \left[y - \left(e_b + \frac{h_c}{2} + \frac{h_{f1}}{2} \right) \right] dy. \quad (9.43a)$$

Again substituting $\sigma_{xx}^{(b)}$ from (9.41b) and performing the integration results in M_d^* in the form

$$M_d^* = M_d - C_3 M_b, \quad (9.43b)$$

where

$$C_3 = \frac{E_{f1}}{D_b} \frac{h_{f1}^3}{12}. \quad (9.43c)$$

The corresponding moment M_s^* in the substrate part is obtained from equilibrium, Figure 9.21b,

$$M_s^* = P^* \left(e_s + \frac{h_c}{2} + \frac{h_{f1}}{2} \right) - M_d^*. \quad (9.43d)$$

Referring now to Figure 9.21b, the stresses in the cross-section of the debonded face produced by the tensile load P^* and the bending moment M_d^* are

$$\sigma_{xx} = \frac{P^*}{h_{f1}} + E_{f1} \frac{M_d^*}{D_d} \eta \, ; \qquad -\frac{h_{f1}}{2} \leq \eta \leq \frac{h_{f1}}{2}, \quad (9.44a)$$

$$\sigma_{yy} = \tau_{xy} \simeq 0, \quad (9.44b)$$

where η is the normal coordinate measured from the mid-plane of the debonded face. In Figure 9.21b, the cross-section of the sandwich ahead of the debond front is subjected to vanishing stress and strain. In the region behind the debond front we assume $\varepsilon_{zz} = 0$ (plane strain). It follows that

$$\sigma_{zz} = \nu_{xz}^{(f1)} \sigma_{xx}; \quad \varepsilon_{xx} = \frac{\sigma_{xx} - \nu_{zx}^{(f1)} \sigma_{zz}}{E_{f1}} = \frac{1 - \nu_{zx}^{(f1)} \nu_{xz}^{(f1)}}{E_{f1}} \sigma_{xx}, \quad (9.44c)$$

where $\nu_{xz}^{(f1)}$ and $\nu_{zx}^{(f1)}$ are the Poisson ratios of the debonded (orthotropic) face sheet.

With the J integral path shown in Figure 9.21b, the following expression holds along the vertical path across the debonded face:

$$dJ = W dy - \mathbf{T} \frac{\partial \mathbf{u}}{\partial x} ds; \quad dy = -ds, \quad (9.44d)$$

where W is the strain energy density, $\mathbf{T}$ is the traction vector and $\mathbf{u}$ the displacement vector (Budiansky and Rice, 1973).

Since

$$W = \frac{1}{2}\left(\sigma_{xx}\varepsilon_{xx} + \sigma_{zz}\varepsilon_{zz}\right) = \frac{1}{2}\sigma_{xx}\varepsilon_{xx}; \qquad \mathbf{T}\frac{\partial \mathbf{u}}{\partial x} = -\sigma_{xx}\varepsilon_{xx}, \tag{9.44e}$$

and since $ds = d\eta$, and by use of (9.44c):

$$dJ = -\frac{1}{2}\sigma_{xx}\varepsilon_{xx}ds + \sigma_{xx}\varepsilon_{xx}ds = \frac{1}{2}\sigma_{xx}\varepsilon_{xx}ds = \frac{1-\nu_{zx}^{(f1)}\nu_{xz}^{(f1)}}{E_{f1}}\sigma_{xx}^2 d\eta, \tag{9.44f}$$

Substituting σ_{xx} from (9.44a), we obtain the contribution of the debonded face to the J integral:

$$\begin{aligned} J_1 &= \int_{-\frac{h_{f1}}{2}}^{\frac{h_{f1}}{2}} \frac{(1-\nu_{zx}^{(f1)}\nu_{xz}^{(f1)})}{2E_{f1}}\left(\frac{P^*}{h_{f1}} + E_{f1}\frac{M_d^*}{D_d}\eta\right)^2 d\eta \\ &= \frac{(1-\nu_{zx}^{(f1)}\nu_{xz}^{(f1)})}{2E_{f1}}\left(\frac{P^{*2}}{h_{f1}} + E_{f1}^2\frac{M_d^{*2}}{D_d^2}\frac{h_{f1}^3}{12}\right). \end{aligned} \tag{9.45}$$

Similarly, if we set

$$(EA)_s = E_c h_c + E_{f2}h_{f2}, \tag{9.46a}$$

then the stresses in the cross-section below the debond in Figure 9.21b, which are produced by the compressive force P^* and the bending moment M_s^* are

$$\sigma_{xx} = \begin{cases} -\dfrac{P^*}{(EA)_s}E_c + \dfrac{M_s^* E_c}{D_s}\xi & \text{if } -e_s - \dfrac{h_c}{2} \le \xi \le -e_s + \dfrac{h_c}{2} \\ & \text{[core]} \\ -\dfrac{P^*}{(EA)_s}E_{f2} + \dfrac{M_s^* E_{f2}}{D_s}\xi & \text{if } -e_s + \dfrac{h_c}{2} \le \xi \le -e_s + \dfrac{h_c}{2} + h_{f2} \\ & \text{[lower face]} \end{cases} \tag{9.46b}$$

and

$$\sigma_{yy} = \tau_{xy} \simeq 0, \tag{9.46c}$$

where ξ is the normal coordinate measured from the neutral axis of this cross-section. Again, following the same arguments as before, i.e. that the cross-section of the sandwich ahead of the debond front is subjected to vanishing stress and strain and that in the region behind the debond front we have $\varepsilon_{zz} = 0$ (plane strain), we obtain the the following expression along a vertical path below the debond:

$$dJ = \frac{1}{2}\sigma_{xx}\varepsilon_{xx}ds - \sigma_{xx}\varepsilon_{xx}ds = \frac{1-\nu_{zx}^{(i)}\nu_{xz}^{(i)}}{E_i}\sigma_{xx}^{(i)2}d\xi, \tag{9.46d}$$

where i refers to the core (c) or the lower face sheet (f_2).

Hence the contribution of the vertical path below the debond to the J integral is

$$J_2 = \int_{-e_s-\frac{h_c}{2}}^{-e_s+\frac{h_c}{2}} \frac{(1-\nu_{zx}^{(c)}\nu_{xz}^{(c)})}{2E_c}\sigma_{xx}^{(c)2}d\xi + \int_{-e_s+\frac{h_c}{2}}^{-e_s+\frac{h_c}{2}+h_{f2}} \frac{(1-\nu_{zx}^{(f2)}\nu_{xz}^{(f2)})}{2E_{f2}}\sigma_{xx}^{(f2)2}d\xi. \tag{9.46e}$$

Substituting the corresponding expressions from (9.46b) and performing the integration leads to

$$J_2 = \frac{P^{*2}}{(EA)_s^2}H_1 + \frac{P^*M_s^*}{(EA)_sD_s}H_2 + \frac{M_s^{*2}}{D_s^2}H_3, \tag{9.47a}$$

where

$$H_1 = \frac{1-\nu_{zx}^{(c)}\nu_{xz}^{(c)}}{2}E_ch_c + \frac{1-\nu_{zx}^{(f2)}\nu_{xz}^{(f2)}}{2}E_{f2}h_{f2}, \tag{9.47b}$$

$$H_2 = \frac{1-\nu_{zx}^{(c)}\nu_{xz}^{(c)}}{2}E_ch_c2e_s + \frac{1-\nu_{zx}^{(f2)}\nu_{xz}^{(f2)}}{2}E_{f2}h_{f2}\left(2e_s-h_c-h_{f2}\right), \tag{9.47c}$$

$$H_3 = \frac{1-\nu_{zx}^{(c)}\nu_{xz}^{(c)}}{2}E_ch_c\left(\frac{h_c^2}{12}+e_s^2\right) + \frac{1-\nu_{zx}^{(f2)}\nu_{xz}^{(f2)}}{2}E_{f2}h_{f2}\left[\frac{h_{f2}^2}{3}+\left(\frac{h_c}{2}-e_s\right)\left(\frac{h_c}{2}+h_{f2}-e_s\right)\right], \tag{9.47d}$$

The sum of the two integrals (9.45) and (9.47a) represents the energy release rate since the remaining portions of the path make no contribution to the J integral, i.e.

$$G = J_1 + J_2 \tag{9.48}$$

or

$$G = \frac{(1-\nu_{zx}^{(f1)}\nu_{xz}^{(f1)})}{2E_{f1}}\left(\frac{P^{*2}}{h_{f1}} + E_{f1}^2\frac{M_d^{*2}}{D_d^2}\frac{h_{f1}^3}{12}\right) + \left(\frac{P^{*2}}{(EA)_s^2}H_1 + \frac{P^*M_s^*}{(EA)_sD_s}H_2 + \frac{M_s^{*2}}{D_s^2}H_3\right), \tag{9.49}$$

where H_1, H_2 and H_3 are given in (9.47b–d).